Mitigating cryogenic microcracking in carbon-fibre reinforced polymer composites using negative thermal-expansion nanoparticles functionalized by a polydopamine coating

Mohammad S. Islam [a], Wenkai Chang [a], Zhao Sha [a], Jiawei Wang [a], Shuying Wu [b], L.R. Francis Rose [c], Anthony J. Kinloch [d], Chun H. Wang [a,*]

[a] *School of Mechanical and Manufacturing Engineering, The University of New South Wales, Sydney, NSW, 2052, Australia*
[b] *School of Engineering, Macquarie University, Sydney, NSW, 2109, Australia*
[c] *Defense Science and Technology, Fishermans Bend, VIC, 3207, Australia*
[d] *Department of Mechanical Engineering, Imperial College London, London, SW7 2AZ, UK*

ARTICLE INFO

ABSTRACT

Herein, we report a new method of mitigating cryogenic microcracking in carbon-fibre reinforced-plastics (CFRPs) using a negative thermal-expansion nanomaterial, zirconium tungstate (ZrW_2O_8), to simultaneously reduce the thermal residual stresses and enhance the fracture energy of the epoxy matrix of CFRPs. The results show that 1 wt% of added ZrW_2O_8 nanoparticles functionalized by polydopamine can increase the fracture energy of the matrix material by 140%, reduce the coefficient of thermal expansion by 20% and, more importantly, enhance the interlaminar fracture energy of the resulting CFRP by about 100% at −196 °C. The ZrW_2O_8-modified matrix has been demonstrated to successfully prevent microcracking at −196 °C in a blocked cross-ply CFRP laminate with a $[0_4/90_8/0_4]$ fibre architecture.

1. Introduction

Fibre-reinforced polymer (FRP) composite technology offers a lightweight alternative to the manufacture of the metallic tanks for storing and transporting cryogenic liquids below −150 °C (such as liquid hydrogen at −253 °C, liquid oxygen at −183 °C and liquid natural gas at −162 °C) for spacecraft and aircraft applications [1,2]. Indeed, the current strong interest in space exploration and the drive towards renewable energy to achieve global net zero CO_2 emissions by 2050 have further heightened the demand for large-scale storage and transport of hydrogen, especially employing lightweight storage tanks [3].

Carbon-fibre reinforced-plastic (CFRP) composites, using epoxy resin matrices, are desirable for lightweight storage tanks, due to their high specific strength and stiffness. However, at cryogenic temperatures they develop high residual thermal stresses because of the mismatch of the coefficients of thermal expansion (CTE) between the carbon fibres and the epoxy matrix. Furthermore, epoxy polymers become significantly more brittle at cryogenic temperatures. These effects lead to CFRPs being more susceptible to matrix microcracking at cryogenic temperatures [4,5] than at the temperature of −54 °C experienced by aircraft.

Such cryogenic microcracking in the matrix can create fuel leakage pathways in, and degrade the structural integrity of, CFRP-based fuel-storage structures. As a result, reducing the CTE mismatch and improving the fracture energy of the matrix material and the CFRP are of great significance to the successful deployment of lightweight composite tanks for storing liquid hydrogen and other cryogenic fuels.

One effective method of increasing mechanical strength, stiffness and toughness at cryogenic temperatures is to incorporate nanoparticles into the matrix [4,6–13]. Indeed, our recent research [14,15] has revealed that the addition of a low thermal-expansion nanomaterial, i.e. CuO nanoparticles, to the epoxy matrix was effective in increasing its fracture energy and the interlaminar fracture toughness of the resultant CFRP-epoxy composite at cryogenic liquid nitrogen temperatures. However, a reduction in matrix cracking was only observed [14] when the nanoparticles were coated with polydopamine (PDA) that increased the fracture energy by reducing agglomeration of the nanoparticles, as well as increasing interactions and effective stress transfer with the epoxy matrix. It was considered that, although the PDA-coated CuO nanoparticles were effective in suppressing microcracks by increasing the toughness of the epoxy matrix, their effectiveness in reducing the

---

* Corresponding author.
E-mail address: chun.h.wang@unsw.edu.au (C.H. Wang).

thermal residual stresses in the matrix of the CFRP was limited due the CuO nanoparticles having a positive CTE in two directions, although lower than that of the epoxy matrix.

Therefore, herein, we investigate the potential of ZrW_2O_8 nanoparticles, which have been reported to possess the highest known negative CTE of $-9 \times 10^{-6} K^{-1}$ [16,17], to simultaneously enhance the fracture energy and to reduce the thermal residual stresses in the matrix of the CFRP, and thus to mitigate matrix microcracking in CFRPs at cryogenic temperatures. Several important aspects are investigated in detail. Firstly, the fibre filtering effect that is often observed during infusing an epoxy resin containing nanoparticles into dry carbon-fibre fabrics has been investigated to identify the critical conditions for obtaining a uniform distribution of nanoparticles in the cured CFRP laminates. Secondly, the ZrW_2O_8 nanoparticles, with and without a coating of PDA, are dispersed in the epoxy resin and the tensile properties and the fracture energies of the cured epoxy polymers are measured at room temperature and at $-196\ ^\circ C$. The PDA-coating of ZrW_2O_8 nanoparticles is studied due to its ability to increase the interfacial interactions with epoxy resin to enhance thermomechanical properties, as well as its ability to reduce agglomeration of the nanoparticles [14,18–20]. The unmodified and modified nanocomposite epoxies are then used to manufacture, using a resin infusion process, CFRP laminates with a $[0_6/\pm35_2/0_6]$ fibre architecture, with the centre stack of $[\pm35_2]$ plies representing laminates of pressure vessels made by the filament winding method. The tensile properties and the interlaminar fracture energy of these CFRPs are measured at room temperature and at $-196\ ^\circ C$. Finally, we have also studied the effectiveness of the uncoated and PDA-coated ZrW_2O_8 nanoparticles in suppressing microcracks in a CFRP with a blocked cross-ply $[0_4/90_8/0_4]$ fibre architecture at $-196\ ^\circ C$.

2. Experimental details

2.1. Materials

An epoxy resin, which was a mixture of diglycidyl ether of bisphenol A and F (Raku Tool, EL-2203) and an amine curing agent (Raku Tool, EH 2970-1) were procured from GMS Composites, Australia, and used to manufacture bulk epoxy and CFRP composite laminate specimens. The shelf life of the epoxy resin is greater than 24 months at $20\ ^\circ C$. The recommended epoxy to curing agent ratio was 1:0.3. After mixing with the curing agent, the epoxy resin has a viscosity of 400–600 mPa $\bullet$ s at $25\ ^\circ C$, making it suitable for resin infusion and filament winding. The gel time of the mixed resin is 1.0 h at $25\ ^\circ C$. By curing at $25\ ^\circ C$ for 12 h followed by post-curing at $120\ ^\circ C$ for 14 h the epoxy can reach a glass transition temperature, T_g, of between $110\ ^\circ C$ and $120\ ^\circ C$.

The ZrW_2O_8 nanoparticles with 99.5% purity were obtained from Changsha Easchem Co. Ltd, China. When a PDA-coating for the nanoparticles was required, the ZrW_2O_8 nanoparticles and a 2-amino-2-(hydroxymethyl) propane-1,3-diol (TRIS) buffer solution (0.26 g) were mixed with dopamine monomer (0.6 g) in 200 mL of water at $30\ ^\circ C$. Then 1.2 g of ZrW_2O_8 nanoparticles were added to the solution and mechanically stirred for 12 h to complete the *in-situ* polymerisation and the formation of a PDA layer on the ZrW_2O_8 nanoparticles through π-π stacking interactions. The detailed procedure is discussed in our previous study [14]. All the CFRP laminates manufactured in the current study were prepared using unidirectional (UD) carbon fibre fabrics (Toray CK 1223JL, 205 GSM) from Allnex Composites, Australia.

2.2. Manufacturing processes

2.2.1. The bulk epoxy polymers

Nanoparticles were weighed to achieve the required concentration before being added to the epoxy resin. The nanoparticles and the epoxy resin were mixed using a three-roll mill with a speed of 100 rpm. The epoxy/nanoparticle mixture was then mixed manually for 10 min with the curing agent, with an epoxy to curing agent ratio of 1:0.3. The epoxy/nanoparticle/curing agent mixture was then degassed using a vacuum pump to give a pressure of 0.95 atm for 30 min before being used to make tensile test specimens (using a rubber mould) or test specimens to measure the fracture energy, $G_{IC, bulk}$, of the bulk epoxy-nanoparticle polymers, both as described below. Tensile test specimens of the unmodified (i.e. neat) epoxy polymer and the epoxy polymer containing different concentrations (i.e. 0.5, 1, 4 and 8 wt%) of uncoated ZrW_2O_8 nanoparticles were manufactured in accordance with the Type IV specimen configuration of ASTM D638 [21]. To assess the fracture energy, $G_{IC, bulk}$, of the bulk epoxy polymers, double cantilever beam (DCB) adhesively-bonded joint tests were prepared and tested in accordance with ISO 25217 [22]. A layer of approximately 2.5 mm in thickness of the unmodified epoxy or the epoxy polymer containing different concentrations of uncoated (i.e. 0.5, 1, 4 and 8 wt%) and PDA-coated (0.5 and 1 wt%) ZrW_2O_8 nanoparticles were used to adhesively-bond two composite adherends. A 12 μm thick and 50 mm long polytetrafluoroethylene (PTFE) film was placed along the mid-plane at one end of the DCB-bonded joint in the epoxy layer to create a pre-crack. The adherends were 2.5 mm thick and were manufactured using 12 plies of unidirectional T700 carbon-epoxy prepreg (VTM264, Lavender Composites, Australia) which were cured and consolidated in accordance with the manufacturer's recommendation (i. e. at $120\ ^\circ C$ and 620 kPa by autoclave processing for 1 h). The surfaces of the cured laminates were abraded using sandpaper (320 grit aluminium-oxide, Norton, Australia) and then cleaned using isopropyl alcohol. The adhesively-bonded joint specimens were then cured at $25\ ^\circ C$ for 12 h and post-cured at $120\ ^\circ C$ for 14 h.

2.2.2. The CFRP composites

Double cantilever beam (DCB) tests using the CFRP laminates were employed to measure the interlaminar fracture energies. To manufacture the CFRP laminates, dry carbon-fibre plies were first cut into pieces 250 mm × 250 mm in size. A total of 16 plies were laid up in a $[0_6/\pm35_2/0_6]$ fibre architecture, where the ply angle of $[\pm35_2]$ is representative of filament winding angles used for making pressure vessels. The plies were placed on a glass table which was waxed to facilitate their removal after curing. A 50 mm long pre-crack was formed by inserting a 12 μm thick and 50 mm long PTFE film between the 8th and 9th ply at one end of the stack. The stack was then assembled with the required bagging materials, including the infusion mesh, peel-ply, breather, and vacuum bag. Resin infusion was then conducted using the unmodified and modified epoxy resins with uncoated and PDA-coated ZrW_2O_8 nanoparticle concentrations of 0.5 and 1 wt% at a vacuum pressure of 0.95 atm. (The epoxy matrix resin formulations containing nanoparticles were prepared as described in Section 2.2.1. However, it should be noted that resin infusion beyond a concentration of 1 wt% ZrW_2O_8 nanoparticles added to the epoxy matrix resin was unsuccessful due to filtering effects, which are discussed later.) After an initial cure at $25\ ^\circ C$ for 12 h, the laminates were post-cured at $120\ ^\circ C$ for 14 h. The CFRP sheets were cut into DCB test samples, measuring 200 mm × 20 mm × 3.4 mm, using a 'Multicam' CNC router.

To study matrix cracking in a CFRP laminate at $-196\ ^\circ C$, blocked cross-ply laminates, with a $[0_4/90_8/0_4]$ stacking sequence, were made with an epoxy matrix containing uncoated and PDA-coated ZrW_2O_8 nanoparticles at concentrations of 0.5 wt% and 1 wt% by infusing the unmodified and modified epoxy resins into this fibre architecture. Again, after an initial cure at $25\ ^\circ C$ for 12 h, the laminates were post-cured at $120\ ^\circ C$ for 14 h. These cross-ply laminates were used to study the effectiveness of the ZrW_2O_8 nanoparticles in eliminating matrix microcracks in such CFRP laminates when subjected to cryogenic temperatures. After quenching at the CFRP laminates in liquid nitrogen, i.e., at $-196\ ^\circ C$, for 45 min, optical micrographs of the laminates were taken.

2.3. Material characterization

2.3.1. The bulk epoxy polymers

The microstructures of the as-received and centrifuged ZrW_2O_8 nanoparticles were analysed using a transmission electron microscope (FEI Tecnai G2 20 TEM from the FEI Company, USA). To obtain the TEM micrographs for measuring the diameter and length distributions, the ZrW_2O_8 nanoparticles were dispersed in ethanol containing 1 wt% of a silicone-based surfactant (BYK-345 from BYK, Germany) by sonicating for 30 min. The viscosity of the epoxy resins with different as received ZrW_2O_8 nanoparticle concentrations was measured using a Brookfield Viscometer (model DV2T Viscometer- HA) with 10–100% torque range was supplied by Brookfield AMETEK Inc., USA.

The coefficients of thermal expansion (CTE) of the as-received ZrW_2O_8 nanoparticles were characterized using X-ray diffraction (XRD) at different temperatures, using a PAnalytical instrument (PANalytical Empyrean 1) equipped with a temperature controllable cryostage, which was supplied by Malvern Panalytical Ltd, UK. Powder diffraction patterns at 27 °C, and then at decreasing temperatures from −13 °C to −253 °C, at intervals of 60 °C with the temperature being held steady for 300 s at each testing temperature, were collected over the 2θ range of 10–60° in a step angle of 0.02°. The Rietveld refinement was performed for each XRD pattern using the HighScore Plus software (supplied by Malvern Panalytical Ltd, UK) which yielded the lattice parameters at different temperatures with R-factors, R_{wp}, from 10.5.0%–12.5%. Within the Rietveld's whole-profile fitting scheme, the experimental XRD profiles were fitted with the most suitable pseudo-Voigt analytical function by adjusting the major parameters including scale factors, background terms, unit cell parameters, profile parameters, and atomic coordinates. The CTE, α, value then can be determined from the XRD patterns according to:

$$\alpha = \frac{1}{\ell_0} \frac{d\ell}{dT} \tag{1}$$

where ℓ_0 is the initial lattice parameter and $d\ell/dT$ is the rate of change in the lattice parameter with temperature [16].

The CTEs of the unmodified and modified epoxy polymers with uncoated ZrW_2O_8 nanoparticle concentrations of 0.5, 1.0 and 2.0 wt% were measured at liquid nitrogen temperature using a Dantec Q-400 3D Digital Image Correlation (DIC) System with the ISTRA 4D software which was supplied by Dantec Dynamics, Denmark. One surface of each of the specimens was painted white on which black speckles were created using black spray-paint. The specimens were placed inside a cryobath testing chamber so that the painted surface faced an optical window on one side of the chamber. The speckles were photographed using the DIC system before and after filling the cryobath with liquid nitrogen. Using the ISTRA 4D software, the thermal strain was determined from the displacement field of the speckles.

A universal testing machine (Instron 3369, Australia) was used to carry out tensile tests in accordance with ASTM D638 [21] at a 1.0 mm/min cross-head displacement rate. The tensile testing at liquid nitrogen temperatures (i.e. at −196 °C) was performed by immersing the specimens, which were attached to loading grips, in a liquid nitrogen-filled container before being tested. At least three to five replicate tensile specimens were used for each of the nanoparticle loadings.

Using an Instron universal testing machine (Instron 3369 with a 1.0 kN capacity loadcell), the DCB adhesively-bonded composite specimens were initially loaded using a cross-head speed of 1.0 mm/min to generate a naturally sharp pre-crack by extending the initial crack length from the PTFE insert by 10 ± 2 mm, followed by complete unloading. Subsequent re-loading of the pre-cracked DCB specimens were performed by applying a continuously increasing displacement with the same cross-head speed of 1.0 mm/min. The DCB specimens, attached to the loading grips, were immersed in liquid nitrogen prior to

testing to measure the fracture energy at −196 °C. During all the tests, the crack was always observed to follow a stable crack path through the mid-plane of the epoxy layer and therefore always propagated cohesively within the epoxy layer, as reported in our previous work [15]. The values of G_{IC} were calculated using the "corrected beam theory" method as given in ISO 25217 [22].

2.3.2. The CFRP composites

Since infusion of the CFRP dry fabric lay-up was seen to be clearly unsuccessful with more than a 1.0 wt% concentration of ZrW_2O_8 nanoparticles in the epoxy matrix, 1.0 wt% and 2.0 wt% concentrations of uncoated ZrW_2O_8 nanoparticles were chosen to study filtering effects. To determine the fibre-filtering effect of using 1.0 wt% and 2.0 wt% of uncoated ZrW_2O_8 nanoparticles in the epoxy matrix when preparing the CFRP laminates, the unidirectional (UD) carbon fibre fabric was cut (of size 200 mm × 200 mm), weighed and put together in three different ply stacks of 4 plies, 8 plies and 16 plies. The nanoparticle-modified epoxy matrix was then infused into the three different types of stacks (i.e. of 4, 8 and 16 plies). Immediately after the infusion the odd plies of each stack were separated, weighed, and washed with acetone to collect the resin and nanoparticle mixture and discard the carbon fibres. To isolate the ZrW_2O_8 nanoparticles present, the acetone was evaporated off and the epoxy was decomposed at 600 °C for 1 h. The residuals, which consisted entirely of ZrW_2O_8 nanoparticles, were weighed, with the results being used to determine the weight percentage of the nanoparticles present in each ply after infusion.

To measure the mode I, interlaminar fracture energy of the CFRP laminates, DCB tests were carried out in accordance with ASTM D5528-13 [23] using a crosshead speed of 3 mm/min. The DCB tests involved applying a monotonically increasing tensile load to the pre-cracked arms of the specimen fitted with loading tabs. Three specimens were tested for each type of the composite material. On continuation of the loading, the load and displacement values in the first 5 mm of delamination growth were recorded in approximately 1 mm crack growth increments. Subsequently, load and displacement data were recorded at increments of 5 mm growth, until the delamination crack had propagated at least 45 mm from the tip of the pre-crack. Afterwards, measurements were taken at every 1 mm increment of crack growth for the last 5 mm of delamination propagation, up to a total delamination length of 50 mm beyond the initial tip of the pre-crack. The initiation fracture energy, $G_{IC, \text{initiat}}$, of the CFRP laminates was determined using the point at which the load had reached a maximum value and the average propagation fracture energy, $G_{IC, \text{s-s prop}}$, was determined by taking the average fracture energy over a crack growth of between 15 and 50 mm of the R-curve. The fracture surfaces of the composites after testing were examined using a FEI Nova Nano SEM 230 field-emission scanning electron microscope supplied by FEI Company, USA.

As noted above, cross-ply laminates with a $[0_4/90_8/0_4]$ stacking sequence were made with an epoxy matrix containing uncoated and PDA-coated ZrW_2O_8 nanoparticles at concentrations of 0.5 wt% and 1 wt% by infusing the unmodified and modified epoxy resins into this fibre architecture. The laminates were used to study the effectiveness of the ZrW_2O_8 nanoparticles in eliminating matrix microcracks in CFRP laminates when subjected to cryogenic temperatures. After quenching at the CFRP laminates in liquid nitrogen, i.e. at −196 °C, for 45 min, optical micrographs of the laminates were taken.

3. Results and discussion

3.1. Physical characterization of ZrW_2O_8 nanoparticles and ZrW_2O_8 nanoparticle modified epoxy polymers

The typical morphology of the as-received ZrW_2O_8 nanoparticles is shown in Fig. S1. (See Section S1 of the 'Supplementary Materials') The width and length distribution of the as-received nanoparticles are given in Fig. 1Sb and 1Sc. We measured the width by taking the average of the

Table 1
Centrifuging parameters.

Particle diameter	Density of ZrW$_2$O$_8$ (g/cm^3)	RPM (rpm)	Time (s)	Particles collected from
50 nm	5.09	12000	245	Precipitant
100 nm	5.09	12000	61	Supernatant + Precipitant
500 nm	5.09	12000	2.45	Supernatant

shortest distances across the particles, and the length by taking the average of the longest distances across the particles. The two-parameter (i.e. the scale parameter, c, and shape parameter, k) version of the Weibull distribution function was used for modelling the length, l, and width, w, of the ZrW$_2$O$_8$ nanoparticles (in nm) which (with for f(l), $c = 170.6$, and $k = 1.03$) gave a mean length, l, of 168.5 nm and which (with for f(d), $c = 112.5$ and $k = 1.06$) gave a mean width, w, of 109.7 nm. No specific shape of the nanoparticles was obvious although the smaller nanoparticles were nearly spherical in shape. The as-received ZrW$_2$O$_8$ nanoparticles were centrifuged to remove particles greater than 100 nm. The angular velocity and time chosen for the centrifugation process are given in Table 1, along with other parameters and the time of sedimentation for a spherical particle can be found in Ref. [24]. (Sedimentation is the time-dependent deposition of particles due to gravity. For nanoparticles then sedimentation can only be observed by increasing the gravitational field by means of centrifugation. In the present study, we

used different sedimentation times at a constant speed of 12000 rpm to separate and collect the nanoparticles smaller than 100 nm)

For the subsequent studies, the centrifuged ZrW$_2$O$_8$ nanoparticles with most of the particles smaller than 100 nm (i.e. approximately 80%) were used. The typical morphology of the separated ZrW$_2$O$_8$ nanoparticles is shown in Fig. 1a. The width and length distribution of the nanoparticles are given in Fig. 1b and c, respectively. The two-parameter (i.e., the scale parameter, c, and shape parameter, k) version of the Weibull distribution function was again used for modelling the length, l, and width, w, of the ZrW$_2$O$_8$ nanoparticles (in nm) after centrifuging, giving a mean width of 43.5 nm (Weibull distribution f(w): $c = 74.5$ and $k = 1.37$) and a mean length, l, of 68.6 nm (Weibull distribution f(l): $c = 44.6$ and $k = 1.14$). Again, no specific shape of the nanoparticles was obvious although the smaller nanoparticles were nearly spherical in shape. Fig. 1d shows the TEM micrographs of the PDA-coating on the ZrW$_2$O$_8$ nanoparticles. The red arrows in the figure indicate the PDA-coating whose thickness was measured to be approximately 3.5 nm.

Fig. 2b shows a cubic crystal lattice of the ZrW$_2$O$_8$ nanoparticle where the lattice parameters are equal and isotropic, i.e. a = b = c, and the lattice angle $\alpha = \beta = \gamma = 90°$ [25]. Data from the XRD measurements are presented in Fig. 2a, from which the lattice constants of the nanocrystals at various temperatures can be calculated from the Rietveld refinement. The results are shown in Fig. 2c, indicating that the lattice parameters of the ZrW$_2$O$_8$ nanocrystals decrease with temperature.
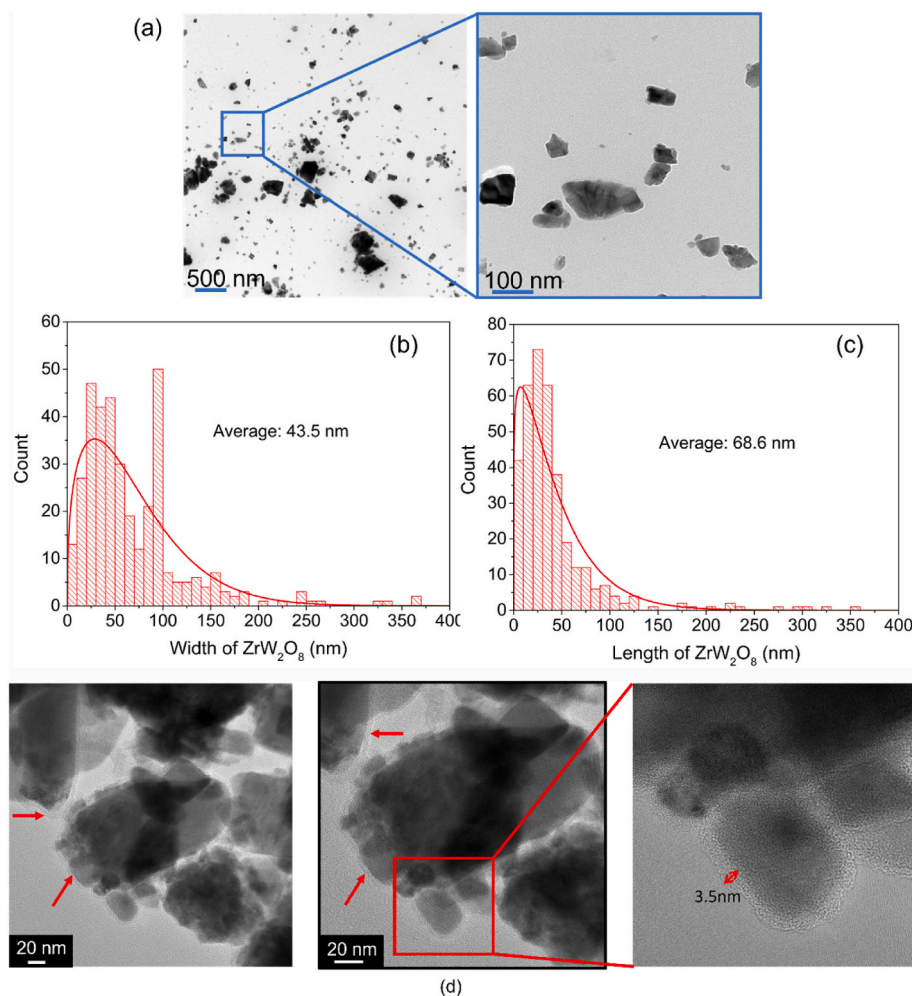

Fig. 1. Characteristics of the ZrW$_2$O$_8$ nanoparticles; (a) TEM micrograph and probability count of (b) width and (c) length correlated with the Weibull distribution; (d) TEM micrographs of the PDA-coating (red arrow) and coating thickness of ZrW$_2$O$_8$ nanoparticles. (For interpretation of the references to colour in this figure legend, the reader is referred to the Web version of this article.)
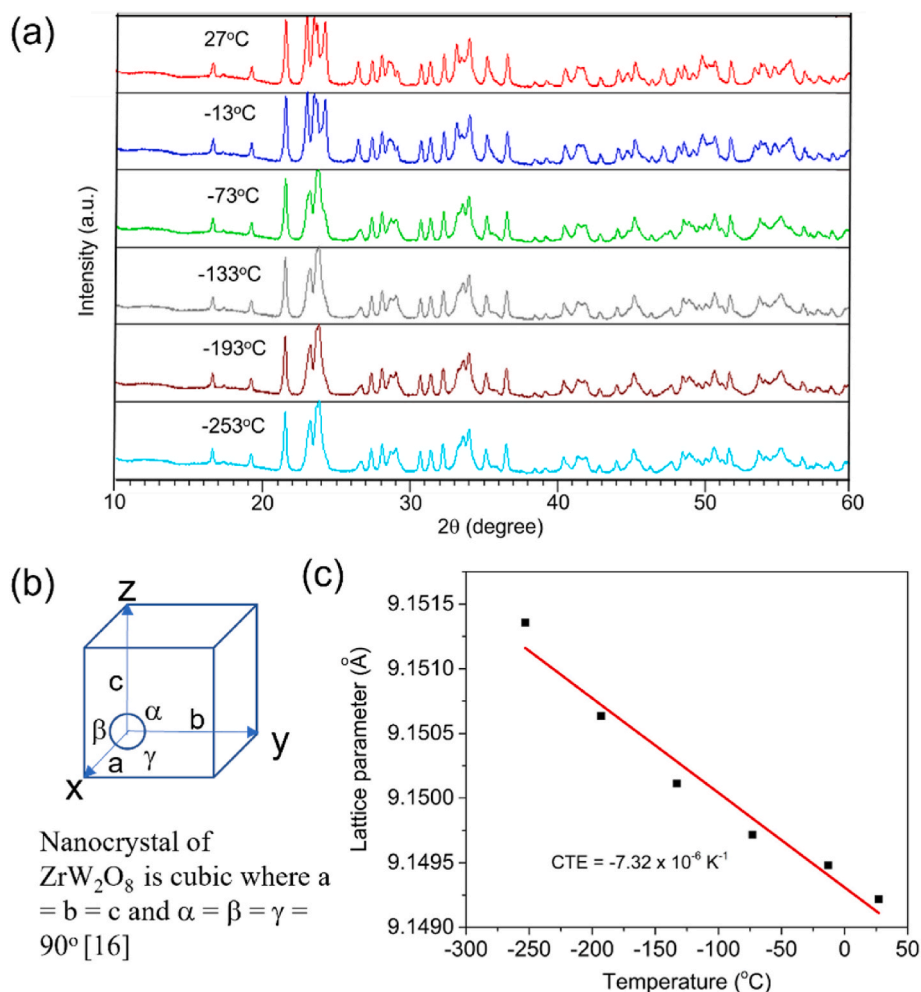
Fig. 2. Thermal expansion properties of ZrW_2O_8 nanoparticles; (a) XRD patterns at various temperatures from 27 °C to −253 °C; (b) a cubic nanocrystal of ZrW_2O_8 showing a = b = c and α = β = γ = 90°, and (c) variation of lattice parameter with temperature.
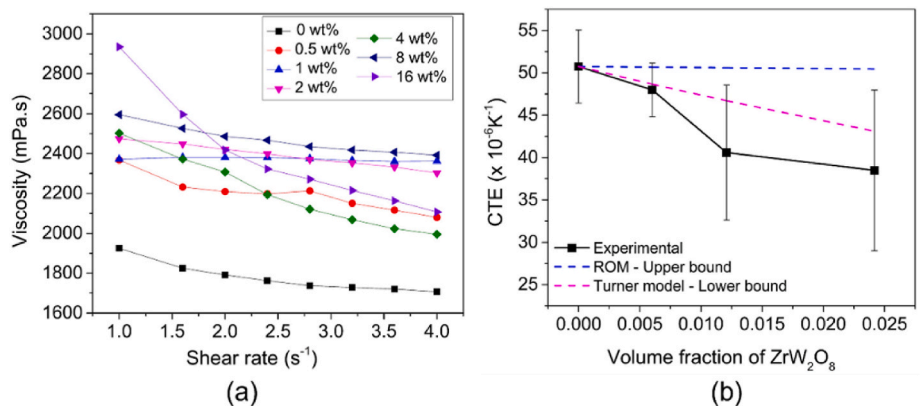

Fig. 3. (a) Viscosity versus shear rate at different ZrW_2O_8 nanoparticle concentrations and (b) a comparison of experimental and rule of mixture (ROM) results for the nanocomposites at different volume fractions of ZrW_2O_8 nanoparticles.

From Fig. 2c the CTE of the ZrW_2O_8 nanoparticles was measured to be -7.32×10^{-6} K^{-1}, which is very close to the value of -9×10^{-6} K^{-1} reported in Ref. [16].

The viscosities, before curing, of the unmodified epoxy resin and the epoxy resin with various concentrations of the uncoated ZrW_2O_8 nanoparticles are presented in Fig. 3a. The results show that adding the nanoparticles increases the viscosity, with the highest viscosity being

observed at the lowest shear rate, indicating a shear-thinning behaviour. This shear-thinning behaviour is most pronounced at the highest nanoparticle concentration, i.e. at 16 wt%. The average viscosity of the epoxy resin modified with ZrW_2O_8 nanoparticles, at various concentrations, lies between 2200 and 2600 mPa s, which is significantly lower than the maximum viscosity allowable [26] for successful infusion of the resin into the reinforcing fibre and fabric, which can be as high as 11000
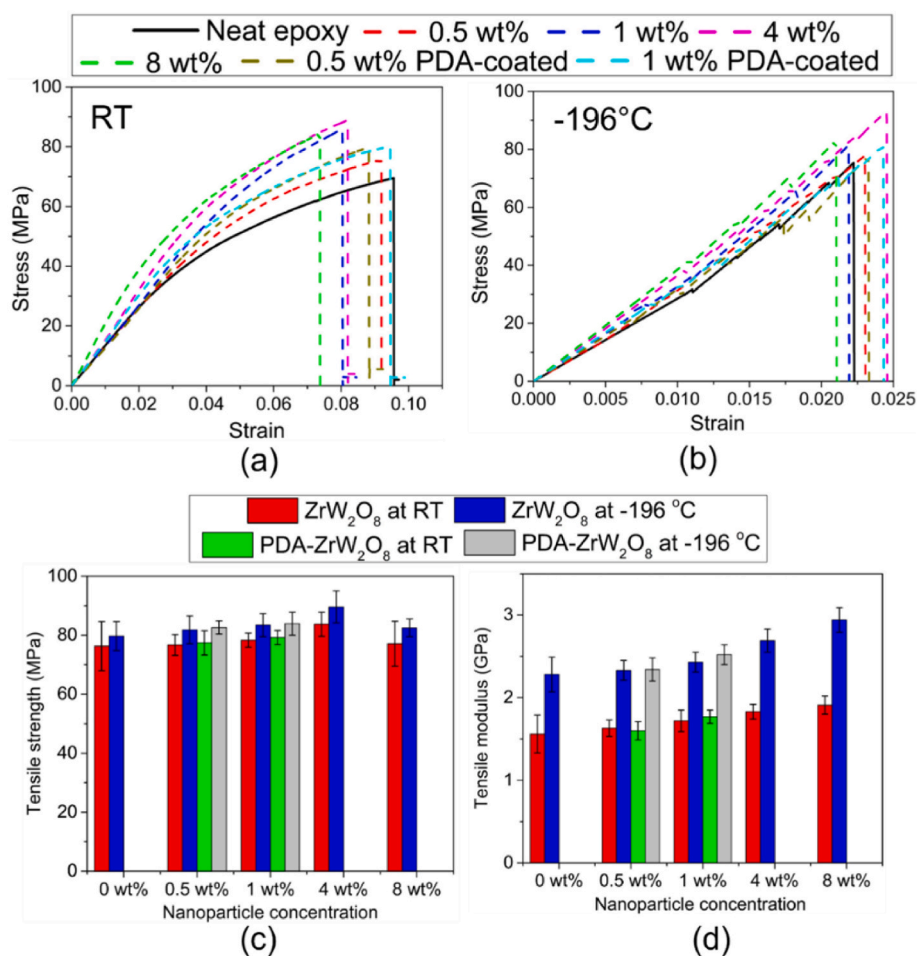
Fig. 4. Typical stress versus strain curves of the epoxy-ZrW_2O_8 nanocomposites at (a) RT and (b) −196 °C; (c) tensile strength and (d) the tensile modulus at different concentrations of uncoated and PDA-coated ZrW_2O_8 nanoparticles.

mPa s. So, in the present study, the viscosity of the unmodified epoxy resin matrix is not an issue, but at high concentrations of nanoparticles the filtering effect becomes a major limiting factor for achieving uniform distribution of the nanoparticles within the composite laminate, which is discussed later in this paper. Fig. 3b shows a comparison of experimental CTE values of the nanocomposites with the results from two theoretical models for the upper- and lower-bounds. Similar to the previous studies [27,28], an upper-bound of the CTE values can be obtained from a rule of mixture (ROM) approach, as given in Eq.S1 [29], and a lower-bound from the Turner model as given in Eq.S2 [30] (see Section S2 of the 'Supplementary Materials'). The estimations of the upper- and lower-bounds from the models were confirmed by the results from previous studies [27,28], from which more details and the relevant model assumptions are available. It can be seen from Fig. 3b that the experimental CTE value of the epoxy-ZrW_2O_8 nanocomposite decreases as the ZrW_2O_8 nanoparticle concentration increases, which is expected as the ZrW_2O_8 nanoparticles possess a negative CTE value. The highest decrease of approximately 25% was seen with a concentration of ZrW_2O_8 nanoparticles of 2 wt%. Furthermore, from Fig. 3b the average experimental CTE values of the unmodified epoxy and epoxy-nanocomposites appear to be generally lower than the CTE values calculated by the lower-bound model of Turner. Using the "Student t-test" (Section S2.1 in 'Supplementary Materials'), the smallest p-value was found to be 0.11, indicating that the mean value of the experimental CTE values is not statistically different from the Turner model prediction. Therefore, the theoretical CTE values from the lower-bound model are in a good agreement with the CTE values determined by the DIC method.

3.2. Tensile properties of the nanocomposites

Typical stress strain curves for the tensile tests at different uncoated and PDA-coated ZrW_2O_8 nanoparticle concentrations at room temperature (RT) and −196 °C are given in Fig. 4a and b, respectively. From the curves a drastic reduction can be seen in the failure strain of 0.02 at −196 °C, compared to 0.08 at RT, which can be considered as a measure or indication of reduced ductility (and increased brittleness) at −196 °C. The epoxy-ZrW_2O_8 nanocomposites show an increasing average tensile strength and Young's modulus as the concentration of nanoparticles is increased at both RT and at −196 °C, except for the specimen with 8 wt % uncoated ZrW_2O_8 nanoparticles whose tensile strength was about the same as that of the unmodified epoxy (see Fig. 4c and d). This may be ascribed to an inadequate dispersion and agglomeration of uncoated ZrW_2O_8 nanoparticles at high concentrations due to the higher viscosity (see Fig. 3a) of the filled epoxy. As shown by the SEM micrographs in Fig. 5a, c and d for the nanocomposite containing 1 wt%, 4 wt% and 8 wt % uncoated ZrW_2O_8 nanoparticles respectively, agglomeration increases with an increase in nanoparticle concentration. The 1 wt% uncoated ZrW_2O_8 nanoparticles has the lowest agglomeration followed by 4 wt% and finally 8 wt% which has the highest nanoparticle agglomeration. Please note that in Fig. 5a, c and d, the purpose is to show only the nanoparticle agglomeration which is highlighted. However, inadequate dispersion with an increase of the nanoparticle concentration is shown in Fig. S2 and is discussed in Section S3 of 'Supplementary Materials'. An increase in the agglomeration of uncoated ZrW_2O_8 nanoparticles is likely to induce high stress concentrations in the nanocomposites and hence a reduction in their tensile strength [31]. Under uniaxial tensile
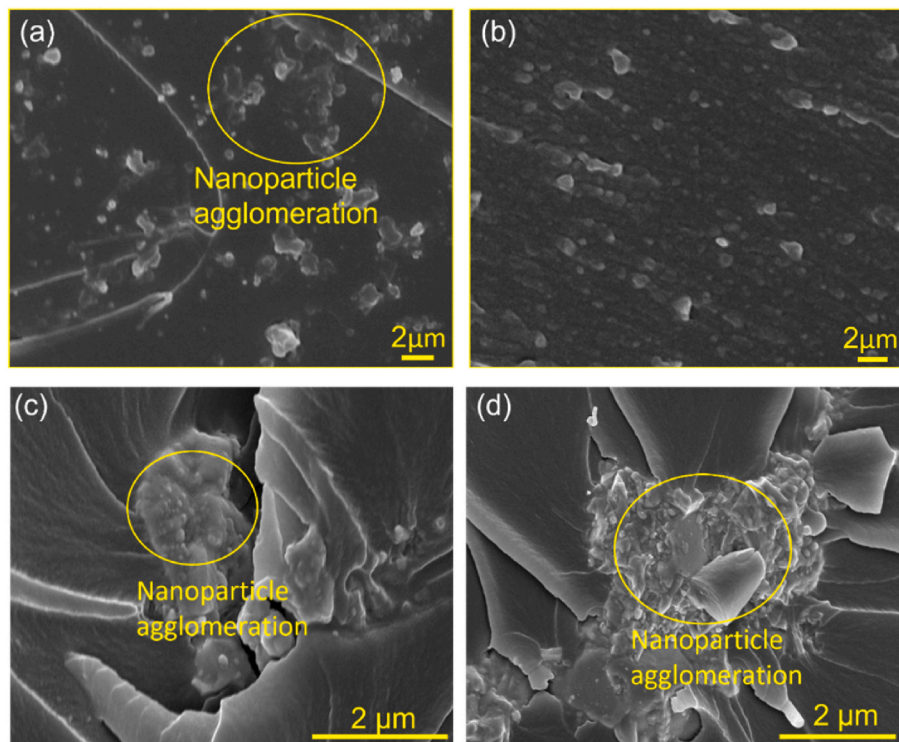
Fig. 5. Distribution of ZrW_2O_8 nanoparticles in the epoxy-ZrW_2O_8 nanocomposites. SEM images of the fracture surfaces of the tensile specimens at $-196\ ^\circ C$ with concentrations of (a) 1 wt% uncoated, (b) 1 wt% PDA-coated, (c) 4 wt% uncoated, and (d) 8 wt% uncoated ZrW_2O_8 nanoparticles.

loading, the nanoparticles in the epoxy nanocomposite samples first debond from the epoxy matrix and then the epoxy matrix between the nanoparticles reaches its static strength causing final rupture. The tensile strengths of the nanocomposite samples are largely determined by the strength of the matrix, which is not affected by the nanoparticles. Therefore, the tensile strengths of the nanocomposites are not very sensitive to the presence of particles. On the other hand, the modulus of the nanocomposites increased slightly with the concentration of uncoated and PDA-coated ZrW_2O_8 nanoparticles, as shown in Fig. 4d. This mainly is due to the fact that at a low stress the particles remain bonded to the matrix, providing some stiffening effects since the stiff particles can transfer the load. This increase in the Young's modulus with the concentration of the nanoparticles is consistent with the expected increase according to the rule of mixtures.

A comparison of the experimental Young's modulus of the uncoated ZrW_2O_8 nanocomposites with the predictions of the upper-bound model showed a satisfactory correlation with the lower nanoparticle concentrations (e.g. a volume fraction of 0.025) but for higher concentrations the modulus values are lower than the upper-bound modulus calculated using the model, which is described in Section S4 of the 'Supplementary Materials'.

3.3. Fracture energy of the epoxy-ZrW_2O_8 nanocomposite polymers

Typical load versus displacement curves of the bonded joint tests of the unmodified epoxy and uncoated ZrW_2O_8-epoxy nanocomposites at RT and $-196\ ^\circ C$ are shown in Fig. 6a and b, respectively. The curves show the shape of a "saw-tooth" indicating typical stick-slip crack growth behaviour. The PDA-coating of CuO was found to improve the fracture energy of the epoxy matrix, and its CFRP laminates, as reported in our previous work [14]. To investigate the potential of a PDA-coating to enhance further the toughening efficiency of ZrW_2O_8 nanoparticles, the same coating method as reported in Ref. [14] was applied to the ZrW_2O_8 nanoparticles, as described above, and the toughness of the resultant nanocomposite was characterized for two concentrations: 0.5

wt% and 1 wt% of ZrW_2O_8. (These two concentrations were selected because, although the fracture energy did increase above 1 wt% of uncoated ZrW_2O_8 nanoparticles, due to the filtering effect no composite laminate could be infused beyond 1 wt%.) Typical load versus crack opening displacement curves for the DCB bonded joint tests of the uncoated and PDA-coated ZrW_2O_8-epoxy nanocomposites at RT and $-196\ ^\circ C$ are shown in Fig. 6c and d, respectively. These curves also show the shape associated with the "saw-tooth" stick-slip crack growth behaviour.

The fracture energy, $G_{IC, bulk}$, of the bulk epoxy polymer for various ZrW_2O_8 nanoparticle concentrations with and without PDA-coating is shown in Fig. 7, with (a) and (b) showing the measured fracture energy versus crack length curves at RT and $-196\ ^\circ C$ for various ZrW_2O_8 nanoparticle concentrations with and without a PDA-coating. The results show that the fracture energy of the bulk epoxy polymer remains approximately constant as the crack propagates through the test specimen, i.e. there is no major increase in crack growth resistance, unlike the case for interlaminar crack growth which will be shown later. Accordingly, an average value of the measured fracture energy, $G_{IC, bulk}$, over the measured crack lengths is employed in Fig. 7c, which is essentially the propagation value of the fracture energy. Thus, Fig. 7c shows the dependence on the concentration of ZrW_2O_8 nanoparticles. In all cases the fracture energy increases with an increasing concentration of ZrW_2O_8 nanoparticles.

Also, the normalized fracture energy, G_{IC} of the nanocomposites, normalized relative to the fracture energy of the unmodified epoxy polymer, versus concentration of nanoparticles is given in Fig. 7d. The fracture energy increases almost linearly with the concentration of nanoparticles up to 8 wt%, reaching the highest improvements of about 150% at RT and at $-196\ ^\circ C$. Overall, the relative improvement in G_{IC} is somewhat more pronounced at $-196\ ^\circ C$ than at RT. A similar observation was also reported in Refs. [15,32] for the addition of SiO_2 nanoparticles and CuO nanorods, respectively, which was ascribed to the influence of thermal residual stresses. PDA-coating of the nanoparticles can further increase the fracture toughness of the nanocomposites
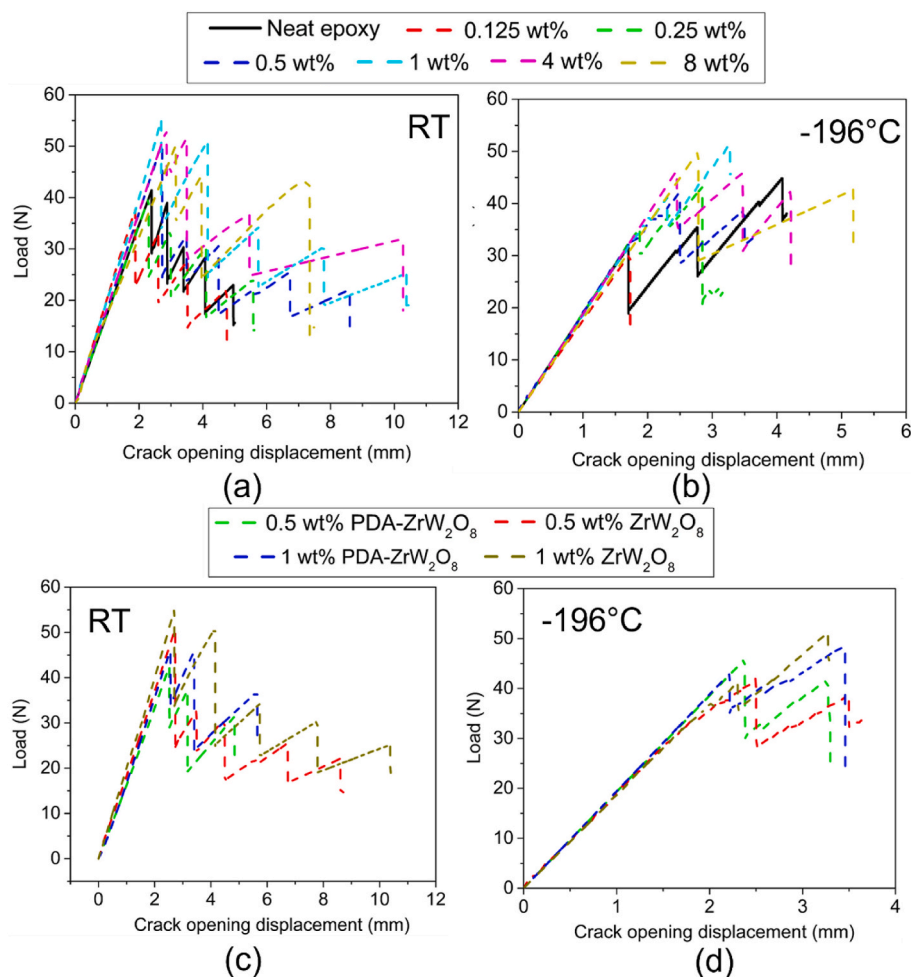
Fig. 6. Load versus crack opening displacement curves of (a) unmodified epoxy and different concentrations (wt%) of epoxy-ZrW_2O_8 nanocomposites at (a) RT and (b) −196 °C. And for uncoated and PDA-coated ZrW_2O_8-epoxy nanocomposites at (c) RT and (d) −196 °C.

compared to the uncoated nanocomposites both at RT and −196 °C, but the improvement was higher at −196 °C as shown in Fig. 7. The highest apparent improvement for a 1 wt% concentration is 140% for the 1 wt% PDA-coated ZrW_2O_8 nanoparticles when tested at −196 °C. Indeed, there is a general trend of an increase in the fracture energy of the bulk epoxy polymer upon PDA-coating the nanoparticles compared with their uncoated counterparts at the same concentration of 0.5 and 1 wt%, both at RT and −196 °C. However, only the 0.5 wt% PDA-coated ZrW_2O_8 nanoparticles at −196 °C showed a statistically significant improvement over the 0.5 wt% uncoated ZrW_2O_8 nanoparticles, as shown by the results of the 'Student t-test' analysis in Table S5 of the 'Supplementary Materials'. To identify potential mechanisms for the toughening effects of uncoated and PDA-coated ZrW_2O_8 nanoparticles, SEM observations were carried out of the fracture surfaces of the test specimens of the epoxy polymer. Our previous publications and other research on nano-toughening of epoxy have found the mechanisms of toughening to include crack-pinning, void growth, microcracking and debonding [14, 15,33]. Fig. 8 shows the SEM micrographs of the fracture surfaces of the epoxy nanocomposites containing 1 wt% uncoated and PDA-coated ZrW_2O_8 nanoparticles at −196 °C. Some crack pinning is visible with void growth on the fracture surface of the 1 wt% uncoated ZrW_2O_8-epoxy nanocomposite (see Fig. 8a), while crack-pinning and river-lines in the matrix, along with larger void growth, microcracking and debonding of the nanoparticles, are more evident on the fracture surface of the 1 wt % PDA-coated ZrW_2O_8-epoxy nanocomposite (see Fig. 8b) [14,15,33]. Fig. 8a also shows that the void size for the 1 wt% PDA-coated ZrW_2O_8 nanocomposites greatly exceeds that in uncoated nanoparticles. Indeed,

as shown in Fig. 8b, the void diameters for coated nanoparticles were found to be 70% higher than for uncoated nanoparticles. This increased void size can account for the enhanced toughening due to the presence of the PDA-coating, which is also consistent with observations reported in our previous work [14]. However, the precise mechanism for the increased void size due to the PDA-coating is not yet clear and requires further investigation. From the perspective of a cohesive zone model for the interface, it is possible that the PDA-coating increases the critical displacement for interfacial failure and this increase may also lead to more extensive plastic void growth. Fig. 9 illustrates the major toughening mechanisms, including nanoparticle debonding and plastic void growth, and crack pinning and crack deflections by the nanoparticles, as shown in the SEM micrographs in Fig. 8. These mechanisms have previously been reported in our work [14,15] and others [34–36]. In particular, it was reported that the toughening mechanisms of debonding and void growth were more prominent at cryogenic temperature than that at RT [14,15].

The reason for the different levels of improvements seen in the strength/stiffness and fracture energy G_{IC} tests is that the former tensile test specimens failed differently from the crack growth process in the DCB fracture toughness tests. The tensile specimens ruptured when the net section stress reached the strength of the epoxy matrix, which is not affected by the nanoparticles. In the fracture toughness tests, however, the energy dissipation arises from the crack growth being accompanied by a process, energy-dissipating, zone surrounding the crack tip, which is under a very high triaxial stress state. The PDA-coating on the nanoparticles raises the debonding strength, compared to the uncoated
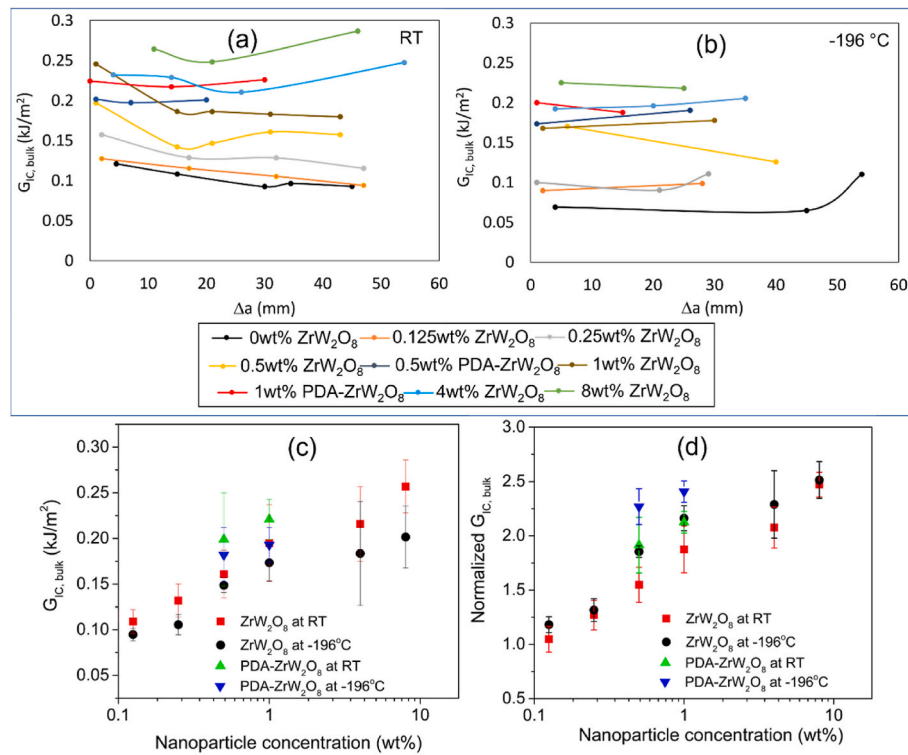
Fig. 7. Typical $G_{IC, bulk}$ values versus crack length curves of epoxy-ZrW_2O_8 nanocomposites with different ZrW_2O_8 concentration (wt.%) with and without PDA-coating and showing no R-curves at (a) RT and (b) −196 °C. The effect of a PDA-coating on the (c) actual and (d) normalized $G_{IC, bulk}$ values of the ZrW_2O_8-epoxy nanocomposites at different ZrW_2O_8 nanoparticle concentrations (wt.%) at RT and −196 °C. (The error bars each correspond to one standard deviation).
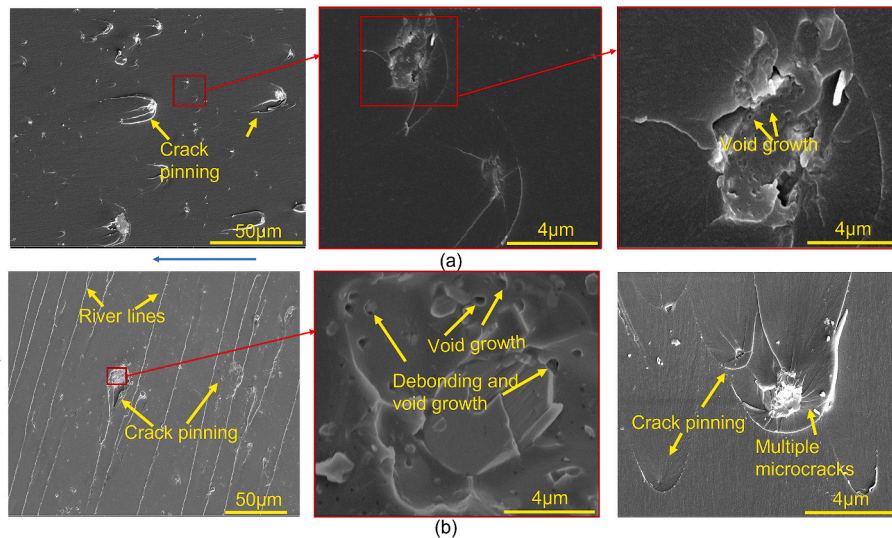

Fig. 8. Fracture surfaces of the epoxy-ZrW_2O_8 nanocomposites containing (a) 1 wt.% ZrW_2O_8 and (b) 1 wt.% PDA-coated ZrW_2O_8 tested at −196 °C. The blue arrows show the direction of crack growth. (For interpretation of the references to colour in this figure legend, the reader is referred to the Web version of this article.)

particles, and thus increases the energy dissipated by void growth. The main increase in the measured fracture energy, G_{IC}, is due to the additional energy dissipated by the nanoparticles inducing shear banding and void growth, as shown by the SEM micrographs of Fig. 8 and the illustration in Fig. 9. By comparison, no void growth was observed on the fracture surfaces of the uniaxially-loaded tensile test specimens shown in Fig. 5.

A comparison of the percentage increase in the $G_{IC, bulk}$ at RT and −196 °C from the addition of uncoated and PDA-coated ZrW_2O_8 nanoparticles with those reported in the literature for other types of

nanoparticles is presented in Fig. 10 [12,35,37]. It is interesting to note that the increase in the fracture energy at −196 °C achieved by the addition of 1 wt% PDA-coated ZrW_2O_8 nanoparticles to the epoxy polymer in the present work, see Fig. 10b, is the highest absolute increase recorded.

3.4. Fibre filtering effect during resin infusion

The 'filtering effect' refers to the phenomenon that carbon fibres can prevent nanoparticles from reaching the interior of the plies due to the
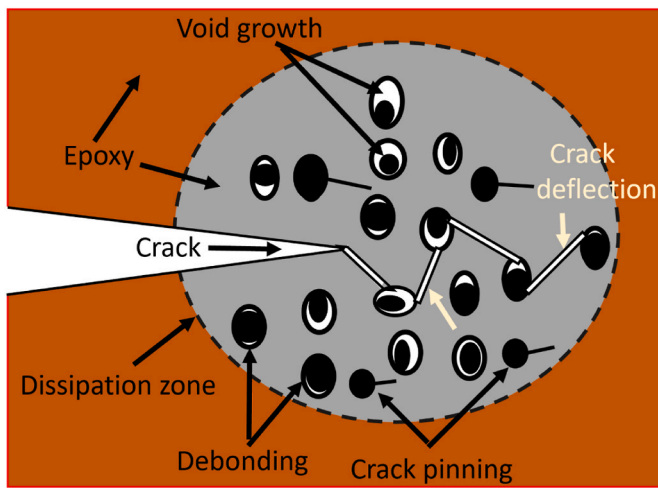
Fig. 9. An illustration showing the major toughening mechanisms including debonding, plastic void growth, crack pinning, and crack deflection in nanocomposites.

small spaces between the fibres. Zhuang et al. [38] measured the average inter-fibre spacing as 1.05 μm, assuming a fibre volume fraction of 60% and an average fibre diameter of 5 μm. Generally, nanoparticles smaller than the inter-fibre spacing should be able to infuse into the fibres but factors such as the nanoparticle aspect ratio, the concentration and degree of agglomeration can influence the fibre filtering effect [39]. This effect can hinder the nanoparticles reaching the interior of fibre plies which results in a reduced nanoparticle concentration in the laminated composites than the original nanoparticle concentration in the resin (see Fig. 11a). Therefore, to measure the fibre filtering effect a 1 wt% and 2 wt% of uncoated ZrW_2O_8-epoxy nanocomposite mixtures were used separately to infuse through 4-ply, 8-ply and 16-ply UD carbon fibre ply stacks so as to measure the fibre filtering effect. Fig. 11b shows the experimental method used and Fig. 11c shows the nanoparticle concentration with respect to the ply position in the laminate stacks for both the 1 wt% and 2 wt% uncoated ZrW_2O_8 nanoparticle concentrations in the epoxy matrix. The 1 wt% ZrW_2O_8-epoxy mixture can infuse through all 4, 8 and 16 plies. Nevertheless, the ZrW_2O_8 nanoparticle concentration was found to be the highest at the surface plies and the lowest in the mid-plies. Since infusion meshes were placed at the top and bottom of the stack, the top and bottom surface plies were found to have the highest ZrW_2O_8 nanoparticle concentration. Further, since all the plies are densely packed and congested, they inhibit the ability of the nanoparticles to move, causing the mid-plies to receive the lowest amount of ZrW_2O_8 nanoparticles. The higher the number of plies in the stack then the lower is the ZrW_2O_8 nanoparticle concentration in

the mid-plies. Furthermore, the filtering effect was more severe with the 2 wt% ZrW_2O_8 nanoparticle concentration. Only the 4-ply and 8-ply stacks were seen to infuse completely with the resin and for the 16-ply stacks only the top four and bottom four plies were seen to be infused. The mid-plies (i.e. ply numbers 5 to 12) were found to be completely dry, i.e. absent of resin, and hence had a zero concentration of ZrW_2O_8 nanoparticles. Therefore, the subsequent study of composite laminates was restricted to laminates where the nanoparticle loading in the matrix was less than, or equal to, 1 wt% of nanoparticles, to ensure adequate resin infusion.

3.5. Fracture energy of the CFRP laminates

The results for the interlaminar fracture energies of CFRP laminates with and without PDA-coated ZrW_2O_8 nanoparticles in the epoxy matrix at RT and −196 °C are presented in Fig. 12 and Tables S6 and S7 (see the 'Supplementary Materials'). It is seen from the resistance (R) curves given in Fig. 12a and b that the interlaminar fracture energies of the laminates increase steadily with the concentration of ZrW_2O_8 nanoparticles. Also, the interlaminar fracture energies of the CFRP laminates with PDA-coated ZrW_2O_8 nanoparticles in the epoxy matrix are higher than those with uncoated ZrW_2O_8 nanoparticles. It is also evident from Fig. 12a and b that the composites exhibit lower interlaminar fracture energies at −196 °C than at RT [40].

The normalized initiation ($G_{IC, initiat}$) and propagation ($G_{IC, s-s prop}$) fracture energies for composites with different nanofillers are shown in Fig. 12c and d, respectively. Also included in Fig. 12c and d are the $G_{IC, initiat}$ and $G_{IC, s-s prop}$ interlaminar fracture energies for the 1 wt% uncoated and PDA-coated CuO nanoparticles which were reported in Ref. [14]. Although improvements in the values of the fracture energies compared with the unmodified laminates are observed at RT and −196 °C, the laminates with the PDA-coated ZrW_2O_8 nanoparticle show a greater improvement compared to those using uncoated ZrW_2O_8 nanoparticles in the matrix, at both RT and −196 °C. At RT, the addition of 0.5 wt% and 1 wt% uncoated ZrW_2O_8 nanoparticles yielded a 10% and 19% improvement in $G_{IC, initiat}$ values, respectively and a 15% and 20% increase in $G_{IC, s-s prop}$ values, respectively, compared with the unmodified-matrix laminate. By contrast, the addition of 0.5 wt% and 1 wt% PDA-coated ZrW_2O_8 nanoparticles to the matrix yielded a 102% and 129% improvement in $G_{IC, initiat}$ values, respectively and a 25% and 55% increase in $G_{IC, s-s prop}$ values, respectively, compared with the unmodified-matrix laminates. At −196 °C, the addition of 0.5 wt% and 1 wt% uncoated ZrW_2O_8 nanoparticles yielded a 15% and 20% improvement in $G_{IC, initiat}$ values, respectively and a 18% and 20% increase in $G_{IC, s-s prop}$ values, respectively, compared with the unmodified-matrix laminate. By contrast, the addition of 0.5 wt% and 1 wt% PDA-coated ZrW_2O_8 nanoparticles yielded a 35% and 55% improvement in $G_{IC, initiat}$ values, respectively, and a 50% and 100% increase in $G_{IC, s-s prop}$ values, respectively compared with the unmodified
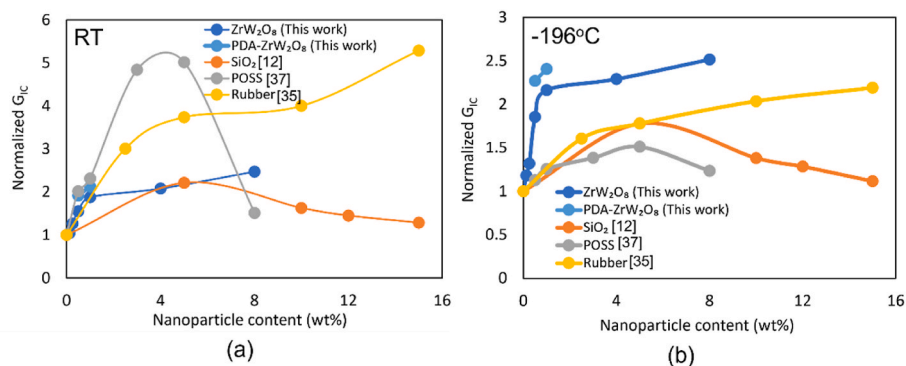

Fig. 10. Comparison of the effectiveness of ZrW_2O_8 nanoparticles in toughening epoxy polymers in comparison with SiO_2 nanoparticles [12], POSS [37] and rubber nanoparticles [35] at (a) RT and (b) −196 °C.
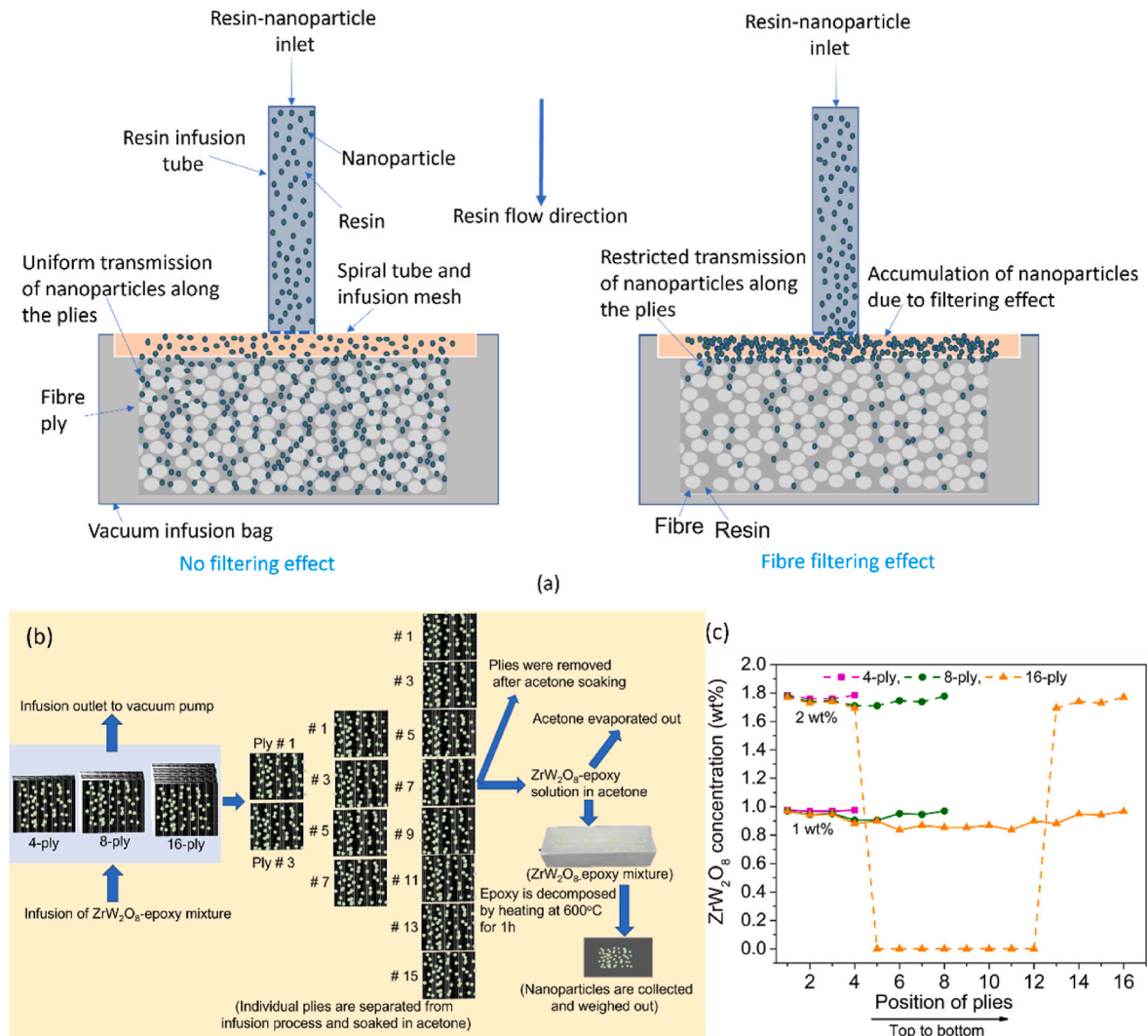
Fig. 11. The effect of the 'fibre filtering effect' from the infusion of an epoxy-ZrW_2O_8 resin matrix into carbon-fibre plies: (a) Display of the fibre filtering effect, (b) characterization method and (c) particle concentration versus ply position in the cured CFRP laminates.

laminate. As reported in Ref. [14], a PDA-coating can enhance the interfacial interactions between the nanoparticles and the epoxy matrix by forming strong bonding at the interface, which may lead to an improved stress transfer and higher interfacial fracture energy, giving rise to the observed increases in fracture energies. The 'Student t-test' analyses in Tables S6 and S7 in 'Supplementary Materials' show that the $G_{IC, initiat}$ and $G_{IC, s-s prop}$ values of the laminates increased significantly for the PDA-coated nanoparticles compared with the uncoated nanoparticles at RT and −196 °C, except for the $G_{IC, s-s prop}$ values for 0.5 wt% nanoparticles in the matrix and tested at RT. For 0.5 wt% nanoparticles at RT, although there was an increase of approximately 10% of the mean values for the PDA-coated ZrW_2O_8 nanoparticles compared with uncoated ZrW_2O_8 nanoparticle matrices, the improvement was not statistically significant. Now, PDA-coated CuO nanoparticles increased the $G_{IC, initiat}$ and $G_{IC, s-s prop}$ values more at −196 °C than that at RT, with a 55% increase in $G_{IC, initiat}$ value and a 10% increase in $G_{IC, s-s prop}$ value at RT and a 115% increase in G_{IC} and 30% increase in the $G_{IC, s-s prop}$ value at −196 °C. Also, compared to the laminates produced with PDA-coated CuO nanoparticles in the epoxy matrix, the PDA-coated ZrW_2O_8 nanoparticles yielded higher $G_{IC, s-s prop}$ values and slightly lower $G_{IC, initiat}$ values.

Significant differences are evident in the fracture surfaces of the laminates with uncoated and PDA-coated ZrW_2O_8 nanoparticles at −196 °C, see Fig. 13. Debonding of individual carbon fibres from the

epoxy matrix and fibre fracture are clearly visible on the fracture surface of the 0.5 wt% and the 1 wt% uncoated ZrW_2O_8-epoxy laminates (see Fig. 13a and c). However, for the PDA-coated 0.5 wt% ZrW_2O_8-epoxy laminates (Fig. 13b), the fibres are mostly covered by the epoxy matrix indicating that the main locus of failure is cohesive fracture in the matrix. Although some fibre-bundle debonding with densely packed fibres was also observed. However, no fibre debonding was visible for the PDA-coated 1 wt% ZrW_2O_8-epoxy laminates but rather cohesive failure in the matrix occurred with feather-like deformation zones, see Fig. 13d. A similar type of feather-like deformations in the polymeric matrix of nanocomposites has been previously reported [32]. These feather-like zones are believed to be due to plastic deformation with localised shear bands [41,42]. Thus, the observed increase in the fracture energy from using the PDA-coated ZrW_2O_8 nanoparticles, compared with the uncoated nanoparticles, may be due to more energy being required to cause matrix cohesive failure and fibre-bundle debonding. This is analogous to the fracture mechanism reported by Zheng et al. for ZnO nanowire-carbon-epoxy laminates [43].

Previous research on the toughening performance of nanofillers in carbon fibre composites [44,45] has found that the constraints imposed by the presence of the carbon fibres can limit the toughening efficiency of nanofillers in the matrix. This leads to any increase in the interlaminar fracture energy of the CFRP laminate being less than the increase in the fracture energy of the bulk matrix when the toughness of the matrix is
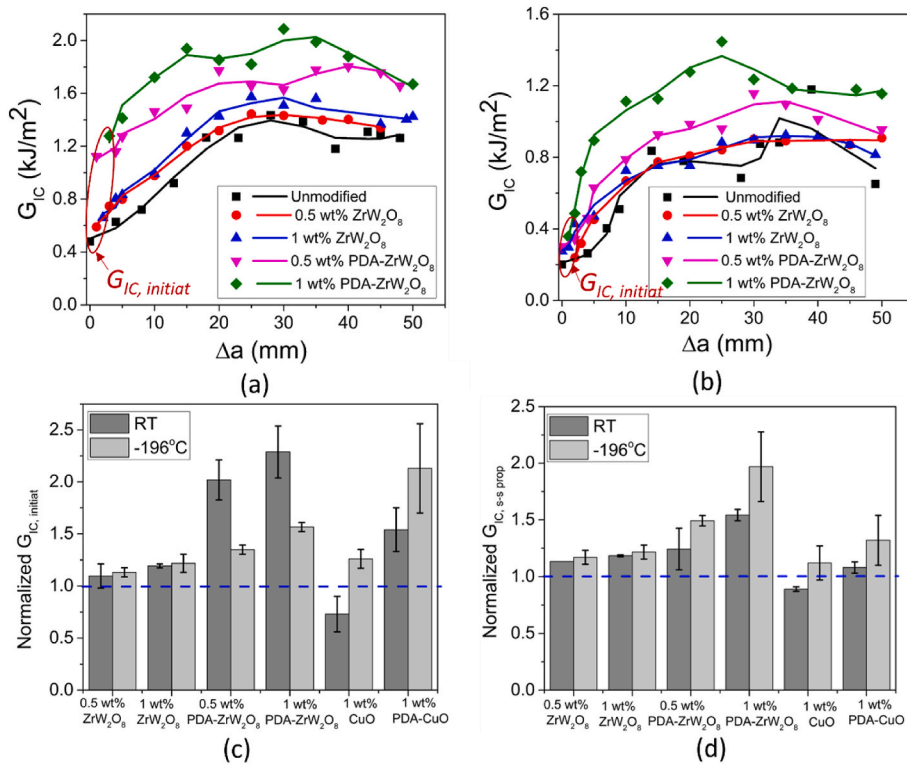
Fig. 12. Typical R-curves for the unmodified and modified CFRP composites at (a) RT and (b) −196 °C, $G_{IC, \, initiat}$ (red circle): first point and $G_{IC, \, s-s \, prop}$: average over a crack growth of 15–50 mm of the R-curves; normalized $G_{IC, \, initiat}$ and $G_{IC, \, s-s \, prop}$ values of the composite laminates at (c) RT and (d) −196 °C. Blue dashed lines show the value of the interlaminar fracture energy of the unmodified epoxy based composites. (For interpretation of the references to colour in this figure legend, the reader is referred to the Web version of this article.)
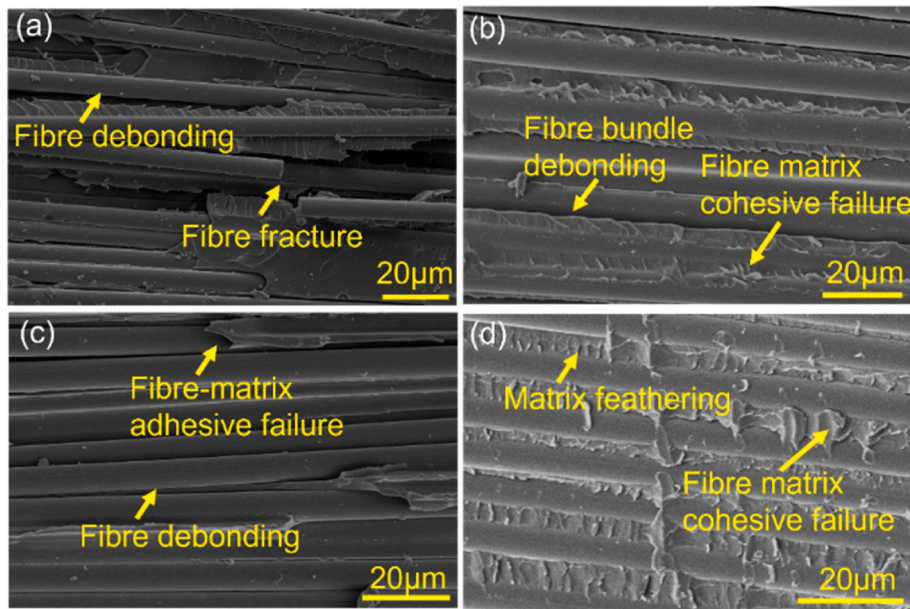

Fig. 13. SEM micrographs of the fracture surfaces of DCB specimens of CFRP composites modified by (a) 0.5 wt% ZrW$_2$O$_8$, (b) 0.5 wt% PDA-coated ZrW$_2$O$_8$, (c) 1 wt% ZrW$_2$O$_8$, and (d) 1 wt% PDA-coated ZrW$_2$O$_8$ nanoparticles. Tests were conducted at −196 °C.

relatively high. In Fig. 14a and b, the measured initiation fracture energies, $G_{IC, \, initiat}$, of the composite laminates are plotted against the corresponding fracture energies, $G_{IC,bulk}$, of the corresponding bulk epoxy polymers. Whilst in Fig. 14 c and d the measured steady-state propagation fracture energies, $G_{IC, \, s-s \, prop}$, of the composite laminates are plotted against the corresponding fracture energies, $G_{IC,bulk}$, of the bulk epoxy polymers. The results shown follow the general trends reported previously [32,46]. For example, initially the slope of the relationships is greater than unity and for the present ZrW$_2$O$_8$ nanoparticle

modified epoxy polymers the initial slope of the relationship is relatively high compared to previous results [32,46]. The increased toughness observed in the CFRP composites, compared to the corresponding bulk polymer, is due to the role of fibre-bridging which can significantly increase the interlaminar fracture energy of the CFRP laminates. Nevertheless, as may be seen from the results for the CuO nanoparticles added to the epoxy polymer [14], when the value of $G_{IC, \, bulk}$, of the bulk epoxy polymer is very significantly increased then this high level of toughness cannot be transferred to the composite laminate due to the constraints
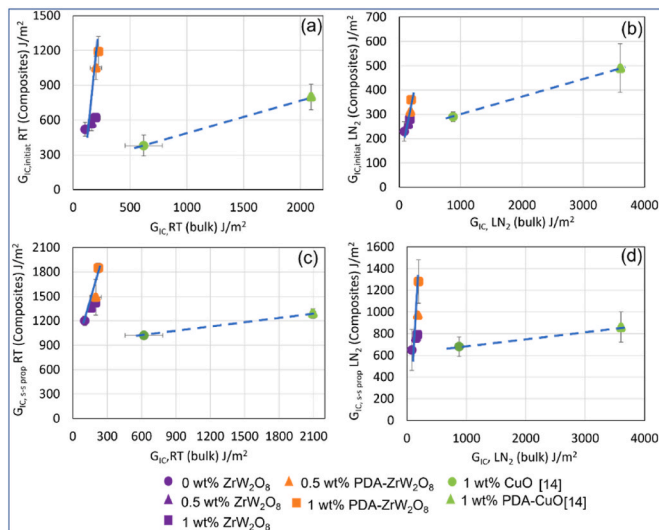
Fig. 14. Comparison of interlaminar fracture energies of the CFRP composites with the fracture energies of the bulk epoxy polymer for different ZrW_2O_8 nanoparticle concentrations (wt%): (a) $G_{IC, initiat}$ values at RT, (b) $G_{IC, initiat}$ values at -196 °C, (c) $G_{IC, s\text{-}s prop}$ values at RT, (d) $G_{IC, s\text{-}s prop}$ values at -196 °C. Solid blue lines indicate the values from the present work and the dashed blue lines indicate values from literature. (For interpretation of the references to colour in this figure legend, the reader is referred to the Web version of this article.)

imposed by the carbon fibres limiting the toughening efficiency of the nanofiller present in the matrix.

Fig. 15 shows the optical micrographs of the blocked cross-ply composite laminates quenched at -196 °C for 45 min and then allowed to equilibrate to room temperature. It is seen that matrix microcracks are visible in the laminate containing the 0.5 wt% uncoated ZrW_2O_8 nanoparticle matrix (Fig. 15a). However, no microcracks can be seen in the laminates with matrices containing either the 1 wt% uncoated ZrW_2O_8 nanoparticles (Figs. 15b), 0.5 wt% PDA-coated ZrW_2O_8 nanoparticles (Fig. 15c) or the 1 wt% PDA-coated ZrW_2O_8 nanoparticles (Fig. 15d). Table 2 summarizes the average microcrack length, as a percentage of the 90° layer ply thickness, for the unmodified CFRP laminates and laminates containing uncoated and PDA-coated ZrW_2O_8 epoxy-nanoparticle matrices from the above tests. The unmodified and 0.5 wt% uncoated ZrW_2O_8 nanoparticle composite laminates are found to contain microcracks of an average length of 81% and 63%, respectively, of the mid-90° layer thickness. On the other hand, no microcracking was visible for the laminates with matrices containing 1 wt% uncoated ZrW_2O_8 or 0.5 wt% and 1 wt% PDA-coated ZrW_2O_8 nanoparticles. From the results shown in Table 2 and Fig. 7 it may be seen that the extent of microcracking that occurs at -196 °C decreases as the fracture energy, $G_{IC, bulk}$, of the epoxy-nanocomposite matrix increases, as measured at -196 °C.

Finally, as a matter of interest, a finite element analysis (FEA) has been undertaken, using a micromechanical model [47], to study the effect of a thermal shock to the composite, i.e., when it is rapidly cooled to -196 °C, compared to the composite being slowly cooled down to an isothermal steady-state at -196 °C. (See Section S6 of the 'Supplementary Materials'.) The thermal residual stresses acting in the matrix were therefore obtained in both the isothermal state (i.e., when the temperature throughout the composite reached -196 °C) and the high temperature gradient during quenching (i.e., when the outer 0° layer was at -196 °C whilst the inner 90° layer was at RT). The modelling studies were undertaken for two different types of matrices: the unmodified epoxy matrix and an epoxy nanocomposite matrix containing 1 wt% of ZrW_2O_8 nanoparticles. The micromechanical model explicitly analyses the thermomechanical deformation of the fibres and the nanocomposite

matrix. The CTEs of the nanocomposite matrix were obtained using the Turner model and the CTEs of the particles measured as given in Fig. 2c, which are shown in Fig. 3b. Using the method reported in Ref. [47], the temperature was varied from the post-curing temperature of 120 °C to room temperature of 25 °C and then down to the cryogenic liquid nitrogen temperature of -196 °C (Fig. S4a in 'Supplementary Materials'). In the isothermal condition the FEA model revealed that the maximum thermal residual stress in the unmodified epoxy matrix and the modified epoxy matrix (i.e., with 1 wt% ZrW_2O_8) reached 36.2 MPa and 28.1 MPa, respectively. Under the quenching (thermal shock) state, the FEA model showed that the maximum transient thermal stress in the unmodified epoxy matrix and modified epoxy matrix reached 36.4 MPa and 28.3 MPa, respectively, which are only approximately 0.6% higher than the values pertinent to the isothermal state. The reason for this small difference is because the temperature gradient has very little effect due to the effective CTE of the CFRP plies in the fibre direction being close to zero. Therefore, the transient thermal stresses in the matrix associated with a thermal shock were found to be very small and would not be a major influence on the presence, or not, of microcracking.

4. Conclusion

We have investigated the effectiveness of a negative CTE nanomaterial, i.e. ZrW_2O_8 nanoparticles, in improving the fracture resistance of a bulk epoxy polymer and CFRP composites made using these epoxy polymers as matrices. Tests have been conducted at room temperature and at cryogenic temperatures. We have demonstrated, for the first time, that ZrW_2O_8 nanoparticles can reduce the CTE of an epoxy matrix, thus lowering the residual thermal stress in the CFRP composite. Furthermore, and perhaps more significantly, the ZrW_2O_8 nanoparticles have been found to increase the fracture energy of the epoxy matrix, which in combination with a reduced CTE of the matrix, can mitigate microcracking in the corresponding CFRP at a cryogenic liquid nitrogen temperature of -196 °C. Based on the results of thermal-mechanical, tension, and fracture tests at RT and -196 °C the following conclusions can be drawn:

1. The CTE of ZrW_2O_8 nanoparticles, measured by XRD crystallography, is found to be -7.32×10^{-6} K^{-1} in the temperature range of 20–300 K. This negative CTE of the ZrW_2O_8 nanoparticles is effective in reducing the CTE of the epoxy matrix of the CFRP at cryogenic temperatures. The ZrW_2O_8 particles have been found to be very effective in improving the fracture energy of epoxy nanocomposites at both room and cryogenic temperatures.
2. Coating the ZrW_2O_8 nanoparticles with polydopamine (PDA) has been highly effective in further improving the fracture properties of epoxy nanocomposites. A 1 wt% of PDA-coated ZrW_2O_8 nanoparticles can improve the fracture energy by up to 140% compared with that for an unmodified epoxy polymer.
3. Incorporating PDA-coated ZrW_2O_8 nanoparticles in the epoxy matrix can dramatically improve the interlaminar fracture energies of the CFRP composites. A 1 wt% addition can increase the initiation and propagation fracture energy of an angle-ply CFRP composite [0_6/$\pm35_2$/0_6] by 130% and 55% at room temperature, and 55% and 100% at -196 °C, respectively.
4. By reducing the CTE and improving the fracture energy of the epoxy matrix, we have demonstrated that the laminates produced with matrices containing 1 wt% uncoated ZrW_2O_8 nanoparticles and only 0.5 wt% of PDA-coated ZrW_2O_8 nanoparticles can effectively suppress matrix cracking at cryogenic liquid nitrogen temperatures.

CRediT authorship contribution statement

Mohammad S. Islam: Conceptualization, Methodology, Validation, Formal analysis, Investigation, Writing – original draft. **Wenkai Chang:** Methodology, Validation, Investigation. **Zhao Sha:** Methodology,
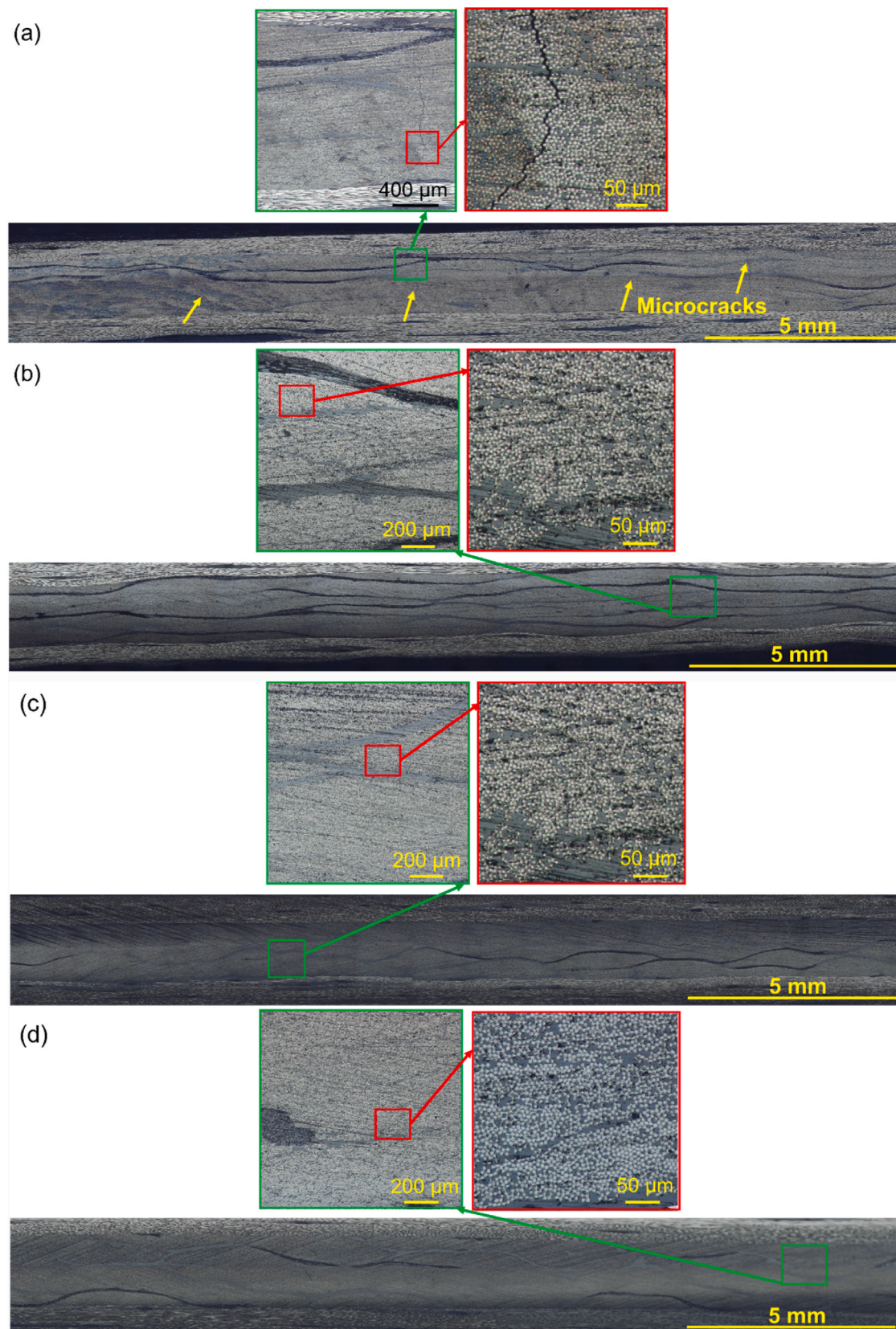
Fig. 15. Optical micrographs of CFRP composite laminates quenched to liquid nitrogen temperature at −196 °C: (a) microcracks in laminates with 0.5 wt% ZrW_2O_8 nanoparticles in the epoxy matrix and no microcracks in laminates with (b) 1 wt% ZrW_2O_8, (c) 0.5 wt% PDA-coated ZrW_2O_8, and (d) 1 wt% PDA-coated ZrW_2O_8 nanoparticles in the epoxy matrix.

Table 2
The percentage of the microcrack length observed in the mid-90° ply thickness of unmodified and modified CFRP composite laminates (after exposure to −196 °C).

Type of epoxy matrix	Microcrack length in the mid-90° ply thickness (%). Layup used: $[0_4/90_8/0_4]$
Unmodified	81 ± 13
0.5 wt.% ZrW_2O_8	63 ± 15
1 wt.% ZrW_2O_8	0
0.5 wt.% PDA-ZrW_2O_8	0
1 wt.% PDA-ZrW_2O_8	0

Investigation. **Jiawei Wang:** Methodology, Investigation. **Shuying Wu:** Conceptualization, Writing – review & editing. **L.R. Francis Rose:** Methodology, Validation, Writing – review & editing. **Anthony J. Kinloch:** Validation, Writing – review & editing. **Chun H. Wang:** Conceptualization, Methodology, Supervision, Project administration, Writing – review & editing.

Declaration of competing interest

Data availability

Data will be made available on request.

Acknowledgements

Appendix A. Supplementary data

Supplementary data to this article can be found online at https://doi.org/10.1016/j.compositesb.2023.110676.

References

[1] Liu N, Ma B, Liu F, Huang W, Xu B, Qu L, Yang Y. Progress in research on composite cryogenic propellant tank for large aerospace vehicles. Compos Appl Sci Manuf 2021;143:106297.

[2] Qiu Y, Yang H, Tong L, Wang L. Research progress of cryogenic materials for storage and transportation of liquid hydrogen. Metals 2021;11:1101.

[3] Bouckaert S, Pales AF, McGlade C, Remme U, Wanner B, Varro L, D'Ambrosio D, Spencer T. Net zero by 2050: a roadmap for the global energy sector, vol. 9. Paris: Rue de la Federation; 2021, 75015. France International Energy Agency.

[4] Chen Z-K, Yang J-P, Ni Q-Q, Fu S-Y, Huang Y-G. Reinforcement of epoxy resins with multi-walled carbon nanotubes for enhancing cryogenic mechanical properties. Polymer 2009;50:4753–9.

[5] Kalia S, Fu S-Y. Polymers at cryogenic temperatures. Springer; 2013.

[6] He Y, Chen Q, Yang S, Lu C, Feng M, Jiang Y, Cao G, Zhang J, Liu C. Micro-crack behavior of carbon fiber reinforced Fe3O4/graphene oxide modified epoxy composites for cryogenic application. Compos Appl Sci Manuf 2018;108:12–22.

[7] Yang J-P, Yang G, Xu G, Fu S-Y. Cryogenic mechanical behaviors of MMT/epoxy nanocomposites. Compos Sci Technol 2007;67:2934–40.

[8] Huang C, Fu S, Zhang Y, Lauke B, Li L, Ye L. Cryogenic properties of SiO_2/epoxy nanocomposites. Cryogenics 2005;45:450–4.

[9] Shen X-J, Liu Y, Xiao H-M, Feng Q-P, Yu Z-Z, Fu S-Y. The reinforcing effect of graphene nanosheets on the cryogenic mechanical properties of epoxy resins. Compos Sci Technol 2012;72:1581–7.

[10] Qu C-B, Huang Y, Li F, Xiao H-M, Liu Y, Feng Q-P, Huang G-W, Li N, Fu S-Y. Enhanced cryogenic mechanical properties of carbon fiber reinforced epoxy composites by introducing graphene oxide. Compos Commun 2020;22:100480.

[11] Li J, Peng C, Li Z, Wu Z, Li S. The improvement in cryogenic mechanical properties of nano-ZrO 2/epoxy composites via surface modification of nano-ZrO_2, vol. 6. Royal Society of Chemistry Advances; 2016. p. 61393–401.

[12] Li S, Chen D, Gao C, Yuan Y, Wang H, Liu X, Hu B, Ma J, Liu M, Wu Z. Epoxy-functionalized polysiloxane/nano-SiO_2 synergistic reinforcement in cryogenic mechanical properties of epoxy and carbon fiber reinforced epoxy laminate. Compos Sci Technol 2020;198:108292.

[13] Jia L, Qi P, Shi K, Liu X, Ma W, Lin S, Zhang F, Jia X, Cai Q, Yang X. High performance epoxy-based composites for cryogenic use: a approach based on synergetic strengthening effects of epoxy grafted polyurethane and MWCNTs-NH_2. Compos Sci Technol 2019;184:107865.

[14] Islam MS, Benninger LF, Pearce G, Wang C-H. Toughening carbon fibre composites at cryogenic temperatures using low-thermal expansion nanoparticles. Compos Appl Sci Manuf 2021;150:106613.

[15] Chang W, Rose LRF, Islam MS, Wu S, Peng S, Huang F, Kinloch AJ, Wang C-H. Strengthening and toughening epoxy polymer at cryogenic temperature using cupric oxide nanorods. Compos Sci Technol 2021;208:108762.

[16] Badrinarayanan P, Ahmad MI, Akinc M, Kessler MR. Synthesis, processing, and characterization of negative thermal expansion zirconium tungstate nanoparticles with different morphologies. Mater Chem Phys 2011;131:12–7.

[17] Neely LA, Kochergin V, See EM, Robinson HD. Negative thermal expansion in a zirconium tungstate/epoxy composite at low temperatures. J Mater Sci 2014;49: 392–6.

[18] Tran NT, Flanagan DP, Orlicki JA, Lenhart JL, Proctor KL, Knorr Jr DB. Polydopamine and polydopamine–silane hybrid surface treatments in structural adhesive applications. Langmuir 2018;34:1274–86.

[19] Knorr Jr DB, Tran NT, Gaskell KJ, Orlicki JA, Woicik JC, Jaye C, Fischer DA, Lenhart JL. Synthesis and characterization of aminopropyltriethoxysilane-polydopamine coatings. Langmuir 2016;32:4370–81.

[20] Ling Y, Li W, Wang B, Gan W, Zhu C, Brady MA, Wang C. Epoxy resin reinforced with nanothin polydopamine-coated carbon nanotubes: a study of the interfacial polymer layer thickness. RSC Adv 2016;6:31037–45.

[21] ASTM D638-14. Standard test method for tensile properties of plastics. USA: ASTM; 2014.

[22] ISO 25217. Adhesives - determination of the mode I adhesive fracture energy of structural adhesive joints using double cantilever beam and tapered double cantilever beam specimens. 2009. Geneva Switzerland.

[23] ASTM D5528-13-Standard Test Method for Mode. I interlaminar fracture toughness of unidirectional fiber-reinforced polymer matrix composites. USA: ASTM; 2013.

[24] Wilson K, Walker J. Principles and techniques of biochemistry and molecular biology. UK: Cambridge university press; 2010.

[25] Mary T, Evans J, Vogt T, Sleight A. Negative thermal expansion from 0.3 to 1050 Kelvin in ZrW_2O_8. Science 1996;272:90–2.

[26] Jiménez-Suárez A, Campo M, Sánchez M, Romón C, Ureña A. Dispersion of carbon nanofibres in a low viscosity resin by calendering process to manufacture multiscale composites by VARIM. Compos B Eng 2012;43:3104–13.

[27] Hashin Z, Shtrikman S. A variational approach to the theory of the elastic behaviour of multiphase materials. J Mech Phys Solid 1963;11:127–40.

[28] Kerner E. The elastic and thermo-elastic properties of composite media. Proc Phys Soc B 1956;69:808.

[29] Takenaka K. Negative thermal expansion materials: technological key for control of thermal expansion. Sci Technol Adv Mater 2012;13:013001.

[30] Turner PS. Thermal-expansion stresses in reinforced plastics. J Res Natl Bur Stand 1946;37:239–50.

[31] Sun Y, Zhao Y, Wu J, Kai X, Zhang Z, Fang Z, et al. Effects of particulate agglomerated degree on deformation behaviors and mechanical properties of in-situ ZrB_2 nanoparticles reinforced AA6016 matrix composites by finite element modeling. Mater Res Express 2020;7:036507.

[32] Carolan D, Ivankovic A, Kinloch A, Sprenger S, Taylor A. Toughened carbon fibre-reinforced polymer composites with nanoparticle-modified epoxy matrices. J Mater Sci 2017;52:1767–88.

[33] Deng S, Ye L, Friedrich K. Fracture behaviours of epoxy nanocomposites with nano-silica at low and elevated temperatures. J Mater Sci 2007;42:2766–74.

[34] Eskizeybek V, Ulus H, Kaybal HB, Şahin ÖS, Avcı A. Static and dynamic mechanical responses of CaCO3 nanoparticle modified epoxy/carbon fiber nanocomposites. Compos B Eng 2018;140:223–31.

[35] Zhao Y, Chen Z-K, Liu Y, Xiao H-M, Feng Q-P, Fu S-Y. Simultaneously enhanced cryogenic tensile strength and fracture toughness of epoxy resins by carboxylic nitrile-butadiene nano-rubber. Compos Appl Sci Manuf 2013;55:178–87.

[36] Wang H, Sun T, Peng C, Wu Z. Effect of different silane coupling agents on cryogenic properties of silica-reinforced epoxy composites. High Perform Polym 2018;30:24–37.

[37] Mishra K, Gidley D, Singh RP. Influence of self-assembled compliant domains on the polymer network and mechanical properties of POSS-epoxy nanocomposites under cryogenic conditions. Eur Polym J 2019;116:283–90.

[38] Zhuang L, Pupurs A, Varna J, Talreja R, Ayadi Z. Effects of inter-fiber spacing on fiber-matrix debond crack growth in unidirectional composites under transverse loading. Compos Appl Sci Manuf 2018;109:463–71.

[39] Wu S, Ladani RB, Ravindran AR, Zhang J, Mouritz AP, Kinloch AJ, et al. Aligning carbon nanofibres in glass-fibre/epoxy composites to improve interlaminar toughness and crack-detection capability. Compos Sci Technol 2017;152:46–56.

[40] Chen J, Kinloch A, Sprenger S, Taylor A. The mechanical properties and toughening mechanisms of an epoxy polymer modified with polysiloxane-based core-shell particles. Polymer 2013;54:4276–89.

[41] Pearson RA, Yee AF. Influence of particle size and particle size distribution on toughening mechanisms in rubber-modified epoxies. J Mater Sci 1991;26:3828–44.

[42] Bagheri R, Pearson R. Role of blend morphology in rubber-toughened polymers. J Mater Sci 1996;31:3945–54.

[43] Zheng N, Huang Y, Sun W, Du X, Liu H-Y, Moody S, et al. In-situ pull-off of ZnO nanowire from carbon fiber and improvement of interlaminar toughness of hierarchical ZnO nanowire/carbon fiber hydrid composite laminates. Carbon 2016; 110:69–78.

[44] Xu F, Du X-S, Liu H-Y, Guo W-G, Mai Y-W. Temperature effect on nano-rubber toughening in epoxy and epoxy/carbon fiber laminated composites. Compos B Eng 2016;95:423–32.

[45] Tsai S-N, Carolan D, Sprenger S, Taylor AC. Fracture and fatigue behaviour of carbon fibre composites with nanoparticle-sized fibres. Compos Struct 2019;217: 143–9.

[46] Hunston DL, Moulton RJ, Johnston NJ, Bascom W. In: Johnson NJ, editor. Matrix resin effects in composite delamination: mode I fracture aspects in Toughened Composites, vol. 937. ASTM STP; 1987. p. 74–94.

[47] Chang W, Francis Rose LR, Wu S, Kinloch AJ, Wang CH. Increasing crack growth resistance for through-thickness matrix cracking and its role in suppressing ply cracking in thin-ply laminates. Compos Appl Sci Manuf 2022;163:107219.